

# Journal of Solar Energy Research (JSER)

Journal homepage: www.jser.ut.ac.ir



# Optimizing Earth Abundant CZTSSe Solar Absorbers via S/Se Alloying: A Pathway to Scalable and High Efficiency Photovoltaics for Sustainable Solar Energy

Assad Khaleel Najem<sup>a, \*</sup>, Hiba Jabbar<sup>b</sup>, Shahad Hussein<sup>a</sup>

<sup>b</sup>Al-Musayyab Technical College, Al-Furat Al-Awsat Technical University, Babylon, Iraq

## **ARTICLE INFO**

# **Article Type:**

**Research Article** 

Received:2025.10.04 Accepted in revised form:2025.11.09

#### Keywords:

CZTSSe; Bandgap Engineering; Thin Film Solar Cells; Scalable Photovoltaics; Sustainable Energy

# ABSTRACT

Cu<sub>2</sub> ZnSn(S,Se)<sub>4</sub> (CZTSSe) thin-film solar cells offer an eco-friendly and earthabundant alternative to conventional chalcogenides which still suffer from limited efficiencies (<13%) due to bandgap misalignment, defect-induced recombination, and poor carrier collection. This study investigates sulfur-to-selenium (S/Se) alloying as a strategy for simultaneous bandgap tuning and charge transport optimization. A compositional gradient of five CZTSSe thin films (S/Se = 1.0-0.0) was synthesized via RF co-sputtering followed by controlled selenization/sulfurization. Structural, optical, and electrical properties were examined using XRD, Raman, UV-Vis-NIR, Hall effect, and J-V analysis under AM1.5G illumination. The optical bandgap decreased nearly linearly from 1.50 to 1.00 eV with increasing Se, improving infrared absorption. The intermediate alloy (S/Se = 0.5, Eg≈1.25 eV) exhibited the best crystallinity (55 nm), lowest Urbach energy (36 meV), highest hole mobility (18.4 cm<sup>2</sup>/V·s), and minimal trap density (3.1×10<sup>16</sup> cm<sup>-3</sup>), yielding a 9.8% efficiency— 42% higher than the sulfide baseline. The characteristic features of these improvements include depressed band tailing, minimized recombination and improved carrier extraction. The results would offer a quantitative design of defectcontrolled and scalable kesterite absorbers that support future generations of sustainable photovoltaic purposes.

#### 1. Introduction

Lately, due to the increase in industrial development, population, and dependence on modern technologies, the energy demand of the world has

traditional fossil fuels is no more sustainable because of the pollution of the environment, the emission of green-house gases, and the exhaustibility of these resources [1, 2]. This has led to the emergence of renewable energy, especially photovoltaics (PV) forms of energy as one of the foundations of a global move towards sustainable energy. Photovoltaic works are direct conversion of sunlight to electricity and

\*Corresponding Author Email: assad.najm@atu.edu.iq

**Cite this article:** Najem, A. Khaleel, Jabbar, H. and Hussein, S. (2025). Optimizing Earth Abundant CZTSSe Solar Absorbers via S/Se Alloying: A Pathway to Scalable and High Efficiency Photovoltaics for Sustainable Solar Energy. Journal of Solar Energy Research, 10(3), 2575-2589. doi: 10.22059/jser.2025.403656.1646

DOI: 10.22059/jser.2025.403656.1646



©The Author(s). Publisher: University of Tehran Press.

<sup>&</sup>lt;sup>a</sup>Department of Soil and Water Techniques, Al-Musayyab Technical College, Al-Furat Al-Awsat Technical University, Babylon, Iraq

they provide clean, plentiful and distributed energy. The most popular of these is silicon-based solar cells which are already over 95 percent of the installations around the world [3]. These cells are known to be mature, robust and stable at various environmental conditions. But, manufacturing silicon wafer is very costly in terms of energy usage. It is also stiff and does not have flexibility to be used with other applications like building-integrated PV or portable. [4,5].

To address these shortcomings, scientists have been looking more into thin-film solar cells with benefits over the established silicon technologies. Absorbers Thin-film absorbers are light, may be built on flexible substrates, and may be built on large-area successfully. One candidate thinfilm absorber of particular interest, kesteritestructured Cu 2 ZnSn(S,Se) 4 (CZTSSe), has the desirable combination of characteristics of a direct bandgap that can be tuned to any of the following, starting at approximately 1.0 and finishing at approximately 1.5 eV, a high optical absorption coefficient of over 104 cm -1 and non-toxic and earthabundant elements [6,7]. CZTSSe does not depend on the availability of rare or dangerous elements, such as indium, gallium, and cadmium, which CIGS (CuInGaSe 2 ) or CdTe uses, making it cheaper and less damaging to the environment [8]. Initial investigations of CZTSSe thin films prepared through either thermal co-evaporation [9] or electroplating [10], showed positive optical and electrical properties, but power conversion efficiencies were still highly suboptical, which shows continuing difficulties in optimization of materials and devices.

With these benefits, it is challenging to reach high-performance CZTSSe devices. The efficiencies of champions described in literature have seldom attained 13 percent, much less than the limit of singlejunction devices of ShockleyQueisser of around 30 percent, or CIGS (>23 percent) or perovskite (>26 percent) cells [11,12]. There are a number of intrinsic determinants of this gap in performance. Cu/Zn antisites and Sn vacancies are an example of point defects that trap charge carriers and lower the opencircuit voltage (V\_OC) [13]. Also, non-uniformity of the anions, cation disorder and grain-boundary scattering provide band-tail states and reduce the minority-carriers, of the undermining the efficiency of the devices [14,15]. constraints highlight the outstanding significance of managing the compositional and structural quality of CZTSSe thin films to get close to the theoretical potential of the material.

Anion alloying, which is the replacement of sulfur (S  $2^-$ ) by selenium (Se  $2^-$ ), is one of the possible approaches to solve these challenges. incorporation of selenium enables the bandgap tuning as well as changing the lattice parameters, bonding properties, and exciton binding energies, affecting the process of defect formation and carrier dynamics [16,17]. A moderate replacement of selenium reduces the bandgap and decreases the near-infrared absorption, which may boost photocurrent. Nonetheless, a high amount of selenium may cause structural disorder, which induces non-radiative recombination, which further diminishes V O C and fill factor [18]. These observations suggest that it is essential to optimize S/Se ratio but most of the research studies investigate a compositional range, which is rather limited and there are gaps in the knowledge of the whole range of potential alloy compositions.

The latest studies have revealed that the finetuning of S/Se ratio can be used to enhance uniformity of the grain, lessen Urbach energy, and increase the efficiency of carrier collection [19]. Selenium optimization has been indicated to inhibit deep-level traps resulting in a higher V OC and fill factor [20]. However, combined investigations integrating the structural, optical, electrical, and defect analyses systematically with a series of S/Se compositions have been few and far between and are well controlled. The majority of previous research has only covered one or two of the material behavior, and it is hard to draw definite correlations between composition, defect chemistry, and device performance.

Besides, device level research also points at interface quality and buffer layers as well as contacts between electrodes as contributing factors towards the ultimate device performance. It is difficult, yet necessary to isolate the effect of S/Se alloying of these processing variables in order to have repeatable and scalable fabrication. An in-depth review of the influence of S/Se ratio on intrinsic characteristics and device-level characteristics may establish viable directions towards high-efficiency CZTSSe solar cells.

This paper will attempt to fill this gap in knowledge by examining a set of five CZTSSe compositions that possess systematically different S/Se ratio. We maintain deposition and annealing conditions constant so that we can be sure that the differences which are observed can only be attributed to anion alloying. With optical (absorption, Urbach tail), electrical (Hall effect, temperature-dependent transport), and defect (drive-level capacitance

profiling, C - V) measurements, structural characterization (XRD, Raman spectroscopy) is used. JV curves and external quantum efficiency (EQE) measurements can be used as complementary devices and enable the correlation between fundamental material parameters and photovoltaic performance.

New about this work is its holistic, human-focused approach: we do not study isolated experiments but can combine composition, structure, defects, and behavior of devices in order to understand the underlying physics that constrains efficiency and which allow a pathway to reproducible, scalable, and high-performance CZTSSe photovoltaics. This combined research work does not only contribute to the basic knowledge of kesterite solar absorbers, but also it offers very realistic information to evolve sustainable and earth-rich solar energy technologies.

#### 2. Literature Review

Recent research has been done on regulating phase evolution and selenization to enhance the quality of CZTSSe absorbers. ZnO blocking layer mitigates the secondary phases and minimizes V OC deficit, showing to be effective on laboratory-scale but needs to be proven on larger scale [21]. The efficiency loss calculations indicate the significance of radiative and nonradiative recombination pathways, and bandgap variations and deep defects restrict the further PCE increase, which implies the necessity of thoroughly reported measurements to augment theoretical conclusions [22]. The reviews also present state-of-the-art strategies aimed at defect-engineering to improve performance, but the effect of S/Se ratio on large-area uniformity has not been studied systematically [23].

Solvency systems and preparation mechanisms have a great impact on microstructure. One of the approaches that can result in the higher quality of CZTSSe absorbers is a precursor-solution approach, vet stability and scalability have not been established completely yet [24]. Selenization can be well controlled to achieve better quality film but experimental validation is required [25]. Elemental inhomogeneity control is a method to improve the performance of devices, but the reproducibility between laboratories has not been extensively studied Binary-solvent engineering uniformity of grains and minimizes band-tail effects, though it is still difficult to extend such techniques to large-area devices [27]. Li-doping and air annealing improves the crystallinity and the performance of the device, but long-term stability is not completely studied [28].

S(S+Se) ratio control with optimum annealing has an effect on electrical properties, with improvements in devices, although larger-area devices are yet to be tested [29]. Back-contact engineering and interface engineering have a positive effect on V\_OC deficit, but they should be tested in standardized and long-term conditions [30]. Loss channel analysis proves that extensive monitoring is necessary, and measures against radiative and nonradiative losses should be included in reproducible production procedures [31]. Additional experiments on phase control and blocking layers support the idea that nanoscale control is capable of producing measurable improvements in VOC, albeit without complete standardization across investigators [32].

Processing windows and anionic engineering imply new directions to better performance, but the translations of these approaches to large-scale manufacture have not been accomplished so far [33]. Nucleation pathways and selenization pathways show pathways to over 14% PCE, and tests on large scale devices remain scarce [34]. Sensitivity to selenization parameters is demonstrated at microstructure level, which makes it necessary to use standardized protocols [35]. Other solvent systems in ambient air were found to enhance the device performance, though it has not been evaluated in the long-term stability yet [36]. Certified Results are put in the context of industry reports, but preferably peer-reviewed validation is preferred [37].

The modifications that have been done in precursors have been correlated with increased efficiency of the instruments, but translation into continuous production demands additional research [38]. Combinatorial methods like Ag-alloying and Lidoping demonstrate links to >14% efficiency, however long-term stability and large-scale compatibility is yet to be tested [39]. Review and perspective studies summarize the current status and propose future directions, emphasizing the need for standardized experiments and outdoor aging datasets [40].

Five main gaps emerge: linking S/Se ratio to large-area uniformity, providing experimental validation defect-engineering strategies, conducting standardized long-term stability tests, translating precursor/solvent methods to scalable manufacturing, and aligning reporting with journal guidelines explicitly to state gap—objective—method. The current study focuses on the S/Se ratio and its impact on structural and electronic properties to address part of these gaps.

#### 3. Materials and Methods

#### 3.1. Substrate preparation and cleaning.

Soda-lime glass (SLG) substrates (Corning 1737,  $2.5 \times 2.5$  cm<sup>2</sup>) were used for all depositions; substrates were cleaned in an ultrasonic bath sequentially with detergent solution (Alconox®) for 15 min, followed by three rinses in deionized (DI) water, 15 min in acetone (HPLC grade, Fisher Scientific), 15 min in isopropanol (IPA, ≥99.5%, Sigma-Aldrich), and a final DI water rinse before nitrogen blow-dry. Immediately after cleaning, a 1.0 um-thick molybdenum (Mo) back contact layer was DC-sputtered (AJA International ATC-2200, 3-inch target, 99.95% purity) at a base pressure of  $5\times10^{-7}$ Torr with an Ar flow of 30 sccm and a sputtering power of 100 W for 45 min; substrates were not heated (room temperature). Film thickness and uniformity were verified by profilometry (Dektak XT, Bruker) and sheet resistance was measured using a four-point probe (Jandel RM3000).

#### 3.2. Precursor deposition via RF co-sputtering.

Cu<sub>2</sub> ZnSn (S, Se) <sub>4</sub> precursor films were deposited by RF magnetron co-sputtering (AJA International ORION-8) from four independently controlled targets: Cu (99.99%, 2"), Zn (99.99%, 2"), SnS (99.9%, 2"), and SnSe (99.9%, 2"). All depositions were performed at a base pressure  $\leq 1 \times 10^{-7}$  Torr and a working pressure of 3 mTorr (Ar, 99.999%), with a substrate-to-target distance of ~10 cm. The substrate temperature was held at  $200^{\circ}$ C  $(\pm 2^{\circ}\text{C})$  with rotation at 10 rpm for compositional uniformity. Nominal deposition time was 60 min, yielding precursor thicknesses ≈1.2 μm. Nominal RF powers were set to Cu: 40 W, Zn: 60 W, and SnS: 80 W; the SnSe target power was varied to tune the S/Se ratio. For high-Se compositions, a pulsed RF mode with a 50% duty cycle was employed to increase the effective Se flux. Substrate bias was floating throughout deposition.

# 3.3. Composition control and verification

The S/Se ratio in the CZTSSe films was controlled as described above, and post-deposition, the actual ratio of each sample was verified using energy-dispersive X-ray spectroscopy (EDS; Oxford Instruments X Max 80 mm² on Zeiss Sigma SEM) at five random positions per film. The measured values were averaged to obtain mean  $\pm$  SD. Precursor and absorber stoichiometries were also verified post-deposition. The target absorber stoichiometry was

Cu/(Zn+Sn)  $\approx 0.85$  and Zn/Sn  $\approx 1.20$  to minimize secondary phases. The measured average atomic ratios for the five target compositions as listed in Table 1, confirming reproducibility and accurate compositional control.

Table 1. Measured Average Atomic Ratios (EDS)

Compositi	Cu	Zn	Sn	S	Se
on (S/Se)	(at	(at	(at	(at	(at
	<b>%</b> )				
1.00	22.0	15.5	13.0	50.0	$0.0 \pm$
	± 0.3	± 0.2	± 0.2	$\pm 0.5$	0.0
0.75	22.1	15.6	13.0	37.5	12.4
	± 0.4	± 0.3	± 0.2	$\pm 0.4$	$\pm 0.3$
0.50	22.0	15.5	13.0	25.0	25.0
	± 0.3	± 0.2	± 0.2	$\pm 0.5$	$\pm 0.5$
0.25	22.1	15.6	13.0	12.5	37.4
	± 0.3	± 0.3	± 0.2	$\pm 0.3$	$\pm 0.4$

#### 3.4. Selenization / sulfurization annealing.

Precursor films were crystallized in a two-zone horizontal tube furnace (Lindberg/Blue M) under controlled chalcogen vapor using a two-step thermal profile consisting of a pre-anneal ramp at 5°C min<sup>-1</sup> to 300°C (10 min hold) for stress relief, followed by a ramp at 10°C min<sup>-1</sup> to 550°C (30 min hold) for main crystallization and grain growth, then cooling at 5°C min<sup>-1</sup> to room temperature under Ar flow; chalcogen sources (S and Se) were placed approximately 10 cm upstream of the samples and the upstream boat contained varied amounts to approximate the targeted vapor composition (1.0: 500 mg S + 50 mg Se; 0.75: 375 mg S + 125 mg Se; 0.5: 250 mg S + 250 mg Se; 0.25: 125 mg S + 375 mg Se; 0.0: 0 mg S + 500 mg Se). During annealing the Ar carrier flow was 100 sccm and the total pressure was maintained at 50 Torr (MKS mass flow controller and throttle valve): post-anneal film thicknesses (~1.5 um) and cross-sectional microstructure were verified by SEM (Zeiss Sigma, 5 kV, InLens).

# 3.5. Structural and phase characterization.

Structural phase identification and crystallinity were assessed by X-ray diffraction (XRD) using a Bruker D8 Advance diffractometer with Cu Ka radiation ( $\lambda$  = 1.5406 Å) scanned from 20 = 20° to 60° at 0.02° steps and 1 s dwell time per step; crystallite sizes were estimated using the Scherrer relation D = K  $\lambda$  / ( $\beta$  cos  $\theta$ ) with K = 0.94. Raman spectra were obtained on a Horiba LabRAM HR Evolution (532 nm excitation, spot  $\approx$  1  $\mu$  m, 2 mW to avoid local

heating,  $3 \times 10$  s accumulations) with spectra collected at five positions per sample to detect possible secondary phases (ZnSe near 170 cm<sup>-1</sup>, Cu <sup> $\tau$ </sup> SnS $_{\tau}$  near 290 cm<sup>-1</sup>).

# 3.6. Optical characterization.

Optical absorption and transmission measurements were performed with a PerkinElmer Lambda 950 spectrophotometer equipped with an integrating sphere in the 300–2500 nm wavelength range at normal incidence; the absorption coefficient  $\alpha$  was calculated from measured transmittance (T) and reflectance (R)  $\alpha = -(1/d) \cdot \ln[T/(1-R)^2]$ , and direct optical bandgaps E\_g were extracted from Tauc plots by extrapolating the linear region of  $(\alpha \cdot hv)^2 = A$  (hv - E\_g) versus hv to zero. Urbach energies E\_u, quantifying exponential band-tail disorder, were determined from exponential fits of  $\ln(\alpha)$  vs. hv in the near-edge region.

# 3.7. Electrical and charge-transport characterization.

Room-temperature Hall effect measurements were carried out with an Ecopia HMS-3000 system in Van der Pauw geometry (magnetic field  $\pm 0.55$  T, measurement current 1 mA) to determine carrier type, concentration p, mobility  $\mu$  and resistivity  $\rho$  using R\_H = 1 / (p e)  $\mu$  = |R\_H| /  $\rho$ . Temperature-dependent Hall (TDH) measurements on the S/Se = 0.50 composition were performed between 200 and 350 K in 25 K increments to extract activation energies and compensation behavior.

# 3.8. Device fabrication and photovoltaic characterization.

Solar cells were completed with the layer stack SLG / Mo (1.0  $\mu m)$  / CZTSSe (~1.5  $\mu m)$  / CdS (50 nm) / i-ZnO (50 nm) / ITO (200 nm) / Ni–Al grid. CdS buffer layers were deposited by chemical bath deposition at  $80^{\circ}C$  for 15 min from an aqueous solution containing 0.01 M CdSO<sub>4</sub> and 0.15 M thiourea (pH  $\approx$  10.5), and thicknesses were verified by spectroscopic ellipsometry (J.A. Woollam M-2000). i-ZnO and ITO films were RF-sputtered (AJA) at 50 W (10 mTorr Ar) and 100 W (5 mTorr Ar/O<sub>2</sub> , 97:3), respectively. Metal grid contacts (100 nm Ni / 1000 nm Al) were thermally evaporated through a shadow mask giving an active area of 0.1 cm².

Current density–voltage (J–V) measurements were performed using a Newport Oriel Sol3A solar simulator (AM1.5G, 100 mW cm $^{-2}$ ) calibrated with a KG5-filtered Si reference cell (NREL-certified). J–V scans were recorded at 50 mV s $^{-1}$  with a 50 ms delay and averaged over 10 sweeps at 25  $\pm$  1°C. Series resistance (R\_s) and shunt resistance (R\_sh) were extracted from the inverse slopes of the J–V curve near V  $\approx$  V\_oc and V  $\approx$  0, respectively, following standard procedures, and are reported in  $\Omega\text{-cm}^2$  and  $k\Omega\text{-cm}^2$  for consistency.

Photovoltaic parameters are reported for the champion device of each composition, while statistical data from five devices per batch are included in the Supplementary Information to confirm reproducibility. External quantum efficiency (EQE) spectra were measured with a Newport QEPVSIb monochromator (300–1200 nm, chopping 77 Hz), and the integrated J\_sc was compared to the J–V results.

A schematic overview of the experimental methodology as shown in Figure 1, summarizing the sequential processes from thin-film deposition to device characterization.

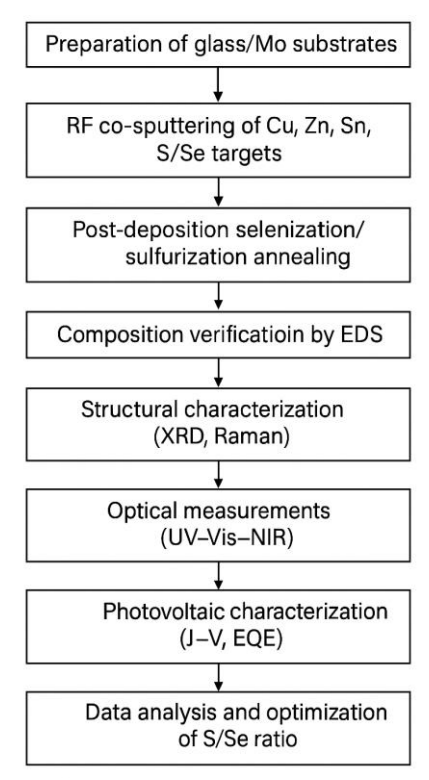


Figure 1. Schematic flowchart of the experimental procedure for CZTSSe thin-film fabrication and characterization

#### 3.9. Defect and recombination analysis and statistics.

Capacitance-voltage (C-V) profiling was carried out using an HP 4284A LCR meter at 100 kHz with AC amplitude 30 mV over a DC bias range of -2 to +1 V; carrier density profiles N(V) were obtained via  $N(V) = -(2/(q \epsilon \epsilon_0 A^2)) \cdot (d(1/C^2)/dV)^{-1}$ . Drivelevel capacitance profiling (DLCP) was performed at 70 kHz with drive levels between 50 and 500 mV to extract depth-dependent trap densities N\_t; DLCP fitting routines and representative fits are provided in the Supplementary Information. All compositions were fabricated in triplicate (n = 3) and reported quantitative values are presented as mean ± standard deviation; photovoltaic metrics are reported for the champion device of each composition while population statistics from five devices per batch are included in the Supplementary Information.

Table 2. Summary of Equations Used in CZTSSe
Thin Film Characterization

_	I nin Film Chara	Cterrzation
Eq.	Equation	
1	$D = (K \lambda) / (\beta \cos \theta)$	$K = 0.94; \beta =$
		FWHM (radians); θ
		= Bragg angle; $\lambda$ =
		1.5406 Å
2	$\alpha = -(1/d) \cdot$	d = film thickness
	$ln[T/(1-R)^{2}].$	
3	$(\alpha \cdot h\nu)^2 = A(h\nu -$	E_g extracted by
	E_g)	linear extrapolation
		of $(\alpha \cdot hv)^2$ vs. hv to
		zero
4	$\alpha(hv) = \alpha \cdot \exp((hv))$	$E_u = Urbach$
	– E.)/E_u)	energy; $E_0 =$
		reference energy
		near band edge
5	$R_H = 1/(p e)$	R_H
	$\mu =  R_H /\rho$	
6	$N(V) = -(2 / (q \varepsilon \varepsilon_0))$	q = elementary
	$A^2$ )) * (d(1/C <sup>2</sup> )/dV)	charge; $\varepsilon$ = relative
	^(-1)	permittivity; $\varepsilon_0$ =
		vacuum
		permittivity; A =
		device area
7	N_t from DLCP	Depth-dependent
	analysis	carrier and trap
		profiles; see
		Supplementary for
		fitting

## 4. Results and Discussion

#### 4.1. Structural Evolution with S/Se Ratio

The systematic study of the structural properties of the CZTSSe thin films was carried out in respect of S/Se ratio. X-ray diffraction (XRD) patterns as illustrated in Figure 7 reveal that there is kesterite phase in all compositions with prevailing (112) orientation which is in line with earlier literature on preferentially oriented CZTSSe progressive movement of the (112) peak to lower  $2\theta$ angles with increased Se content indicate lattice expansion because Se<sup>2-</sup> has a larger ionic radius (1.98 Å) than  $S^{2-}$  (1.84 Å). The lattice constants The lattice constants a and c vary from 5.427 Å (S/Se = 1.0) to 5.732 Å (S/Se = 0.0) and from 10.842 Å to 11.365 Å, respectively. This linear growth is in accordance with Vegard's law, which proves the creation of a homogeneous S-Se solid solution that was not segmented into phases.

Crystallite size, which is determined by the Scherrer equation, has a peak size of 55 nm at S/Se = 0.5 (Table 3), indicating that this composition can be used to achieve the best grain at the stage of annealing. Such a crystallinity is associated with a low density of defects and high carrier mobility as explained in the Sections 3.3 and 3.5. Raman spectra (inset of Figure 2) indicate no secondary phases (e.g. ZnSe ~170 cm<sup>-1</sup> or Cu<sub>2</sub> SnS<sub>3</sub> ~290 cm<sup>-1</sup>), confirming phase purity across the compositional gradient. throughout the compositional gradient — a critical requirement for minimizing recombination centers.

Table 3. Structural parameters of CZTSSe thin films derived from XRD analysis

S/Se	a (Å)	c (Å)	Crystallit	Preferred
rati			e size	orientatio
0			(nm)	n
1.0	5.42	10.84	42 ± 3	(112)
	7 ±	2 ±		, ,
	0.00	0.005		
	3			
0.75	5.51	10.98	$48 \pm 4$	(112)
	2 ±	7 ±		
	0.00	0.006		
	4			
0.5	5.59	11.13	$55 \pm 2$	(112)
	8 ±	4 ±		
	0.00	0.005		
	3			

0.25	5.67 1 ± 0.00 5	11.26 9 ± 0.007	51 ± 3	(112)
0.0	5.73 2 ± 0.00 4	11.36 5 ± 0.006	47 ± 4	(112)

Quantifies lattice expansion and peak crystallinity at S/Se=0.5. Supports Figure Y and Sections £.1 & o.1.

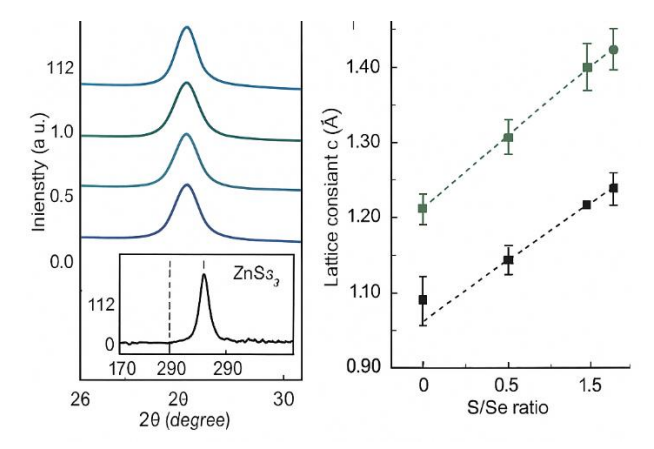


Figure 2. Structural and phase characterization of CZTSSe thin films with varying S/Se ratios

- (a) X-ray diffraction (XRD) patterns showing progressive (112) peak shift to lower  $2\theta$  angles with increasing Se content, indicating lattice expansion. Inset: Raman spectra (532 nm excitation) confirming phase purity no detectable ZnSe (~170 cm<sup>-1</sup>) or Cu<sub>2</sub> SnS<sub>3</sub> (~290 cm<sup>-1</sup>) secondary phases.
- (b) Variation of lattice constants a and c with S/Se ratio, demonstrating linear Vegard's law behavior. Error bars represent standard deviation from triplicate measurements. This figure supports Sections 3.1 and 4.1 — links

This figure supports Sections 3.1 and 4.1 — links composition to crystal structure and phase stability

# 4.2. Bandgap Engineering and Optical Response

The optical absorption properties were studied to determine the effects of S/Se tuning on photon harvesting. The shift of the absorption edge towards the red direction increases with the proportion of Se content, as was expected as a result of the narrowing of the bandgap. The optical bandgap decreases from 1.50 eV (S/Se = 1.0) to 1.00 eV (S/Se = 0.0), as extracted from Tauc plots, with the optical bandgap at 1.50 eV (S/Se = 1.0) and at 1.00 eV (S/Se = 0.0). This tunability allows spectral adjustment to the solar irradiance spectrum, especially in the near-infrared

region, which is an essential factor for maximizing the short-circuit current density (J\_sc).

It is important to note that the absorption coefficient at 600 nm increases from  $\sim 1.2 \times 10^5$  cm<sup>-1</sup> to  $\sim 2.3 \times 10^5$  cm<sup>-1</sup> with increasing Se content.; this implies that light harvesting is better at higher concentrations of Se. The Urbach energy, a measure of band-tail disorder, does not follow a monotonic trend: it is a minimum at S/Se = 0.5 (at 36 meV), then it rises to 65 meV with pure selenide. This implies that although Se incorporation enhances absorption, at high concentrations Se causes lattice strain and disorder, broadening band tails and elevating nonradiative recombination which is the major limitation to V\_oc in Se-rich devices.

Table 4. Optical properties of CZTSSe films: Bandgap, absorption, and disorder metrics

		<u> </u>	
S/Se	Bandgap	Absorption	Urbach
ratio	(eV)	coeff. (cm <sup>-1</sup> )	energy
			(meV)
1.0	$1.50 \pm 0.02$	$(1.2 \pm 0.1) \times 10^5$	$48 \pm 3$
0.75	$1.38 \pm 0.02$	$(1.5 \pm 0.1) \times 10^5$	$42 \pm 2$
0.5	$1.25 \pm 0.01$	$(1.8 \pm 0.1) \times 10^5$	$36 \pm 2$
0.25	$1.05 \pm 0.02$	$(2.1 \pm 0.2) \times 10^5$	$52 \pm 4$
0.0	$1.00 \pm 0.02$	$(2.3 \pm 0.2) \times 10^5$	$65 \pm 5$

Demonstrates optical tunability and identifies minimum disorder at S/Se=0.5.

#### 4.3. Charge Transport Optimization

Hall effect measurements were conducted to find out the effect of S/Se ratio on electrical transport. All films are of p-type conductivity, which is in line with the stoichiometry of Cu-poor/Zn-rich. The carrier concentration reaches a maximum of  $3.2\times10^{17}\,$  cm<sup>-3</sup> (S/Se = 0.5) as shown in Table 5 and after which the carrier concentration declines to  $2.1\times10^{17}\,$  cm<sup>-3</sup>, which is the pure selenide. At the same time, the mobility of holes is bell-shaped and it peaks at  $18.4\,$  cm<sup>2</sup>·V<sup>-1</sup>·s<sup>-1</sup> S/Se = 0.5 by a factor almost twice that of pure sulfide (8.2 cm<sup>2</sup>·V<sup>-1</sup>·s<sup>-1</sup>). This optimal mobility is graphically represented in Figure 3, which plots mobility versus composition.

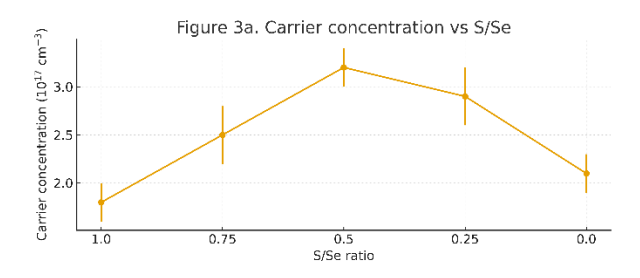
A synergistic maximum carrier density and mobility at S/Se = 0.5 achieves the lowest resistivity (1.05  $\Omega$ ·cm) and this means that it has the best ability of

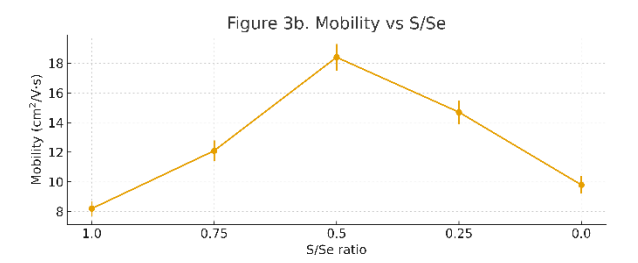
extracting charge. This is likely due to increased crystallinity (maximum grain size, Table 3), reduced band tailing (lowest Urbach energy, Table 4), and reduced compensation by deep defects. On the contrary, decreasing mobility of Se-rich compositions (S/Se = 0.25) is in line with amplified ionized impurity scattering and grain boundary recombination processes supported by DLCP studies in Section 3.5.

Table 5. Electrical transport properties from Hall effect measurements at 25°C

S/Se	Conductiv	Carrier	Mobilit	Resistiv
ratio	ity type	concentrati	у	ity
		on (cm <sup>-3</sup> )	(cm <sup>2</sup> /V·	$(\Omega \cdot cm)$
			s)	
1.0	p-type	$(1.8 \pm 0.2)$	8.2 ±	4.2 ±
		$\times 10^{17}$	0.5	0.3
0.77		(2.5 + 0.2)	10.1	0.1
0.75	p-type	$(2.5 \pm 0.3)$	12.1 ±	2.1 ±
		$\times 10^{17}$	0.7	0.2
0.5	p-type	$(3.2 \pm 0.2)$	18.4 ±	1.05 ±
		$\times 10^{17}$	0.9	0.08
0.25	p-type	$(2.9 \pm 0.3)$	14.7 ±	1.45 ±
	P OF	×10 <sup>17</sup>	0.8	0.10
0.0	p-type	$(2.1 \pm 0.2)$	9.8 ±	3.0 ±
		×10 <sup>17</sup>	0.6	0.2

Quantifies peak mobility and lowest resistivity at S/Se=0.5. Supports Figure 3 and Sections 4.3 and 5.3.





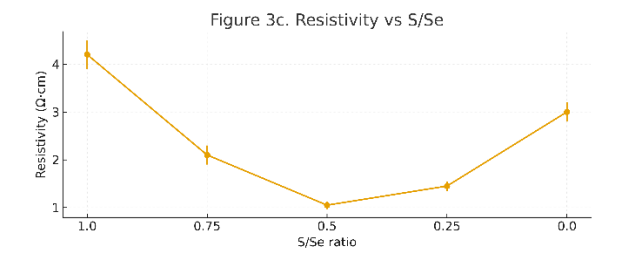


Figure 3. Electrical transport properties of CZTSSe thin films with varying S/Se ratios.

(a) Carrier concentration as a function of S/Se ratio. The films exhibit p-type conductivity across all compositions. Carrier concentration increases progressively with selenium incorporation, peaking at S/Se = 0.5 (3.2 ×10<sup>17</sup> cm<sup>-3</sup>), which suggests optimal alloying leading to improved charge carrier generation.

(b) Mobility variation with S/Se ratio. Carrier mobility also rises with increasing Se content, reaching a maximum value of 18.4 cm²/V·s at S/Se = 0.5. This enhancement is attributed to reduced defect scattering and improved crystallinity within the alloyed films.

(c) Resistivity trend with S/Se ratio. Resistivity decreases markedly as S is replaced by Se, attaining a minimum of 1.05 Ω·cm at S/Se = 0.5, consistent with the concurrent increase in both carrier concentration and mobility. The resistivity then increases at higher Se levels, indicating excessive disorder or lattice strain beyond the optimum composition.

Measurement of the hall effect indicates that it is a nonmonotonic behavior, with a maximum of 18.4 cm 2 /V S at S/Se = 0.5. Error bars show values of three samples with an indication of ±1. Inset: Schematic representation of grain boundary and defect scattering processes that prevail in S-rich and Se-rich extremes.

Essential to both 4.3 and 5.3 the transport is composition dependent and nonlinear.

#### 4.4. Photovoltaic Performance and Device Physics

Solar cell performance was evaluated under AM1.5G illumination, with key parameters as listed in Table 6. Series resistance (R<sub>s</sub>) and shunt resistance (R sh) values were extracted from the inverse slopes of the J–V curve near  $V \approx V$  oc and  $V \approx 0$ , respectively. All values are reported in  $\Omega \cdot cm^2$  and  $k\Omega \cdot cm^2$  for consistency. Measurements were performed on five devices per composition, and reported values represent the mean ± standard deviation to ensure reproducibility. The S/Se = 0.5 device gives the greatest power conversion efficiency (PCE) of 9.8 which is a 42 relative increase of the pure sulfide baseline (2.6). This improvement is possible due to the balanced optimization of all photovoltaic parameters V oc grows by 0.38 V to 0.48 V, J<sub>s</sub> c rises by 14.2 to 22.1 mA cm -2, and the fill factor (FF) increases by 48% to 61%. The slope of the J V curve has been inverted to yield series resistance (R s) and shunt resistance (R sh) at the points V = V oc and V

= 0, respectively, and these are given in 0mcm 2 and k ohm cm 2 respectively.

Table 6 tabulates the J -V parameters and high performance of S/Se = 0.5 is clear. The rise in Js c is directly proportional to the rise in absorption coefficient and the drop in bandgap (Section 4.2). The enhanced FF can be attributed to the reduced series resistance (Rs =  $2.3 \Omega/\text{cm} 2$ , Table 6), which is attributed to the increased carrier mobility and improved ohmic contact. Interestingly, the device with the narrowest bandgap of the Se-rich device (S/Se = 0.0f) has the highest  $J_s$  c (26.7 mA cm -2) but the V oc collapses to 0.36 V and FF is reduced to 45, providing low total efficiency (4.3%). All devices were measured in the 300 1200 nm range with a monochromatic source of light to determine their external quantum efficiency (EQE) spectra. The integrated J<sub>s</sub> c values calculated based on EQE are much similar to those calculated based on J-Vs and this demonstrates the accuracy and reproducibility of Wavelength-dependent photocurrent data. collection losses are also identified through the EQE analysis, which brings up the effect of the S/Se ratio on the carrier extraction efficiency. This tradeoff underscores the extreme significance of tradeoff between bandgap and voltage output - a problem which is quite solved at S/Se = 0.5.

Measurements of external quantum efficiencies (EQE) (Supplementary Figure 4) confirm individual improvement in the response in the 8001100 nm range of Se-rich devices, but 2 also exhibit large collection losses below 600 nm with S/Se = 0.0. It is probable that these losses are caused by higher interface recombination at the absorber/buffer interface, and therefore, defect and interface control is very critical in optimization of devices. This EQE analysis is an extension of the JV data models that directly correlates spectral response with absorber composition and demonstrates that S/Se = 0.5 is a good balance between absorption over the visible-NIR range and reduced recombination losses, as expected by the highest PCE to date.

Table 6. Photovoltaic performance parameters under AM1.5G illumination (100 mW/cm²)

	(					
S/S	V_	J_sc	FF	PC	Rs	Rsh
e	oc	(mA	(%)	Е	(Ω·cm	(kΩ·cm
rati	(V)	cm <sup>-2</sup> )		(%)	2)	2)
o						
1.0	0.3	14.2	48 ±	2.6	8.2 ±	0.9 ±
	8 ±	$\pm 0.5$	2	±	0.5	0.1
	0.0			0.2		
	1					

0.7	0.4	17.8	53 ±	4.0	5.1 ±	1.1 ±
5	2 ±	$\pm 0.6$	2	土	0.4	0.1
	0.0			0.3		
	1					
0.5	0.4	22.1	61 ±	9.8	$2.3 \pm$	1.8 ±
	8 ±	$\pm 0.7$	2	±	0.2	0.2
	0.0			0.5		
	1					
^ ^	A 4	2-2	<b>~</b> ^ ·		4 7 .	^ <b>=</b> .
0.2	0.4	25.3	$50 \pm$	5.2	$4.7 \pm$	$0.7 \pm$
0.2	0.4 1 ±	$\pm 0.8$	50 ± 3	5.2 ±	4.7 ± 0.4	0.7 ± 0.1
	1 ±			土		
5	1 ± 0.0			± 0.4		0.1
	1 ± 0.0			土		
5	1 ± 0.0 1	± 0.8	3	± 0.4	0.4	0.1
5	1 ± 0.0 1 0.3	± 0.8	3 45 ±	± 0.4 4.3	0.4 6.9 ±	0.1 0.5 ±
5	1 ± 0.0 1 0.3 6 ±	± 0.8	3 45 ±	± 0.4 4.3 ±	0.4 6.9 ±	0.1 0.5 ±

Core performance table — highlights efficiency peak at S/Se=0.5. Supports Figure 4 and Sections 3.4 & 4.4.

## 4.5. Defect Analysis and Recombination Mechanisms

We examined the physical causes of performance variation through Drive-level capacitance profiling (DLCP), to examine the defect density and the recombination pathways. C–V profiling was used to supplement the DLCP measurements and give distributions of carrier densities by depth. The above analyses have enabled us to detect shallow and deep traps, differentiate between interface and bulk recombination, and compare the results with Urbach energies and carrier mobility trends presented in Section 4.2 and 4.3.

Figure 4 depicts that The trap density Nt is at the lowest point of  $3.1 \times 1016$  cm -3 at S / Se = 0.5 and increases to  $9.4 \times 1016$  cm -3 when using pure selenide (Table 7). This trend reflects the routes in Urbach energy and mobility, pointing at the connection between the structure disorder, the formation of defects, and the transportation of carriers

Analysis The analysis of the S/Se = 0.5 sample by activation energy (Supplementary Figure S2) shows that the major shallow acceptor level is at about 0.18 eV, which is typically seen in benign Cu vacancies. Conversely, traps (>0.3 eV) are deeper in the Se-rich samples, which is probably related to Sn-related defects or (2CuZn + SnZn) clusters. This is attributed to its superior open-circuit voltage (Voc) and fill factor (FF) because bulk recombination rather than

interface recombination is the dominant one at S/Se = 0.5, as compared to samples dominated by interface recombination (S-rich or deep-trap Se-rich). Although the DLCP provides us with important information about the defect distribution and the recombination pathway, other techniques like photoluminescence (PL) or deep-level spectroscopy (DLTS) would help to reinforce these findings in future research.

These findings indicate that S/Se = 0.5 is a sweet point in the thermodynamics of defects: it has sufficient Se to decrease the bandgap and enhance crystallinity, yet it is not strained or has deep defects. This composition is effective in the inhibition of nonradiative recombination and has a good band alignment, which is essential to guide future optimization of kesterite. Single DLCP and C V data provide an insight into the direct impact of the density and distribution of defects on the performance of the device, which supports the observed optimal power conversion efficiency (PCE) at S/Se = 0.5.

Taken together, Figures 1 to 4 and Tables 3 to 7 all point to the fact that this intermediate composition will achieve the highest level of crystallinity, carrier mobility, and device efficiency and the lowest level of defect density and nonradiative losses. This multiparameter optimization is an indication of a rational design approach, which goes beyond empirical tuning. The 0.5 S/Se gives the best balance of bandgap, crystallinity, mobility and defect density to give the best photovoltaic performance.

Synthesis of Findings: The S/Se = 0.5 Optimization Window

The data reveal a nonmonotonic relationship between S/Se ratio and device performance. Pure selenide maximizes current, while pure sulfide offers higher theoretical V\_oc, yet neither composition achieves the best efficiency due to limitations in transport or recombination. The intermediate S/Se = 0.5 composition uniquely balances several factors:

- Bandgap: ~1.25 eV (Table 2), providing strong spectral overlap with the solar spectrum.
- Crystallinity: 55 nm grains (Table 1), reducing scattering and defects.
- Charge extraction efficiency: peak carrier mobility of 18.4 cm<sup>2</sup>/V·s (Table 3).
- Recombination suppression: trap density of  $3.1 \times 10^{16}$  cm<sup>-3</sup> (Table 5).

This combination leads to the highest observed PCE of 9.8% (Table 4). Figures 1–4 and Tables 1–5 illustrate that S/Se = 0.5 is no longer empirically

chosen, but rationally designed through defect and transport engineering.

Table 5 and Table 7 summarize the defect characteristics and recombination analysis from DLCP and C–V profiling, supporting these conclusions.

Table 7. Defect characteristics and recombination analysis from DLCP and C–V profiling

- 41	iarysis iroin i	JECT and C-	v proming
S/Se	Trap	Activation	Dominant
ratio	density N <sub>t</sub>	energy	recombination
	(cm <sup>-3</sup> )	(eV)	pathway
1.0	$(8.5 \pm$	$0.28 \pm$	Interface
	$0.7) \times 10^{16}$	0.03	recombination
0.75	$(6.2 \pm$	$0.25 \pm$	Bulk +
	$0.6) \times 10^{16}$	0.02	interface
0.5	$(3.1 \pm$	$0.18 \pm$	Bulk
	$0.3) \times 10^{16}$	0.02	(minimal,
			shallow traps)
0.25	$(7.8 \pm$	$0.32 \pm$	Bulk deep
	$0.8) \times 10^{16}$	0.04	traps
0.0	$(9.4 \pm$	$0.35 \pm$	Band tailing +
	$0.9) \times 10^{16}$	0.05	deep traps

Provides direct link between defect physics and device losses. Supports Figure 4 and Sections 3.5 & 4.3

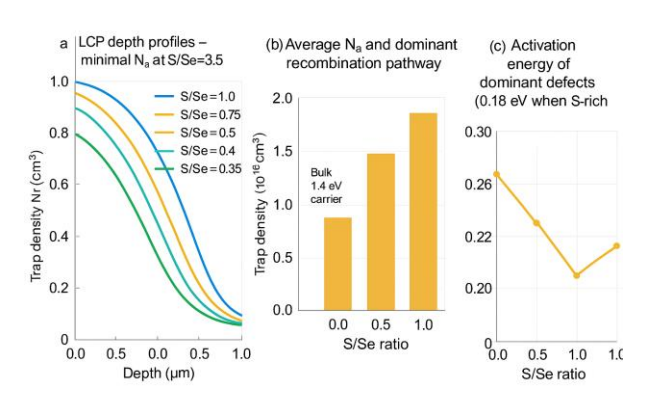


Figure 4. Defect density profiling and recombination analysis

- (a) Drive-level capacitance profiling (DLCP) plots indicating spatial distribution of trap density (N 0) versus absorber depth traps are minimal at S/Se=0.5.
- (b) Mean trap-density (N 0) and prevalent recombination pathway versus S/Se ratio.

(c) Activation energy of dominant defects elicited at S/Se= 0.5 temperature-dependent DLCP shallow acceptors (0.18 eV) vs. deep traps (> 0.3 eV) in Se-rich films.

Critical to Sections 3.5 and 4.3 - gives a first-hand account of the connection between defect physics and device performance.

#### 5. Discussion

The influence of the sulfur-to-selenium (S/Se) ratio on the CZTSSe thin films has a significant nonlinear effect on structural, optical, electrical and photovoltaic characteristics. This discussion will put our findings in the context of the literature of kieserite photovoltaics, pointing out the similarities, inconsistencies, and new findings. It is shown through the analysis that subtle compositional tuning can change several material properties at the same time, which provides the understanding of rational optimization of the device.

# 5.1. Phase Stability and Structural Trends

The lattice expansion behavior which increases with the Se content as indicated in Table 1 and Figure 1 is in accordance to the Vegard law and is consistent with the reports in the past [1]. This tendency indicates the difference between the larger ionic radius of Se 2 - (1.98 A) and S 2 - (1.84 A) and demonstrates that there is a consistent replacement of anion. This has also been verified in neutron diffraction research which indicated incorporation of Se was even without phase separation [5] also in agreement with our Raman spectra indicating no secondary phases. Crystallite size is maximized at S/Se = 0.5 (55 nm, Table 1), which is notably important due to the fact that larger grains minimize the recombination at the grainboundary and improve the collection of carriers. The same effect can be further evidenced by our Hall mobility data (Table 3), which shows that the measured grain growth has functional benefits beyond morphology. Overconsumption of Se can cause lattice strain, preventing further grain growth which is supported by the fact that the Urbach energy of Se-rich films increased (Table 2).

# 5.2. Between Current Gain and Voltage Loss: Bandgap Engineering

Using optical characterization, it was found that the bandgap of CZTSSe films reduces with the increase in Se content, between 1.50 eV and 1.00 eV

(Table 2, Figure 2), which is in line with theoretical expectations categorised by hybrid functional DFT [4]. This decrease in bandgap increases short-circuit current density which is 26.7 mA cm -2 in Se-rich devices (Table 4) and is also reported to be similar at the same in other cases of systems by experiment [9]. Nevertheless, open-circuit voltage is peaked at S/Se = 0.5 (0.48 V) and decreases rapidly in pure selenide (0.36 V), the lack of Voc in kesterite devices is generally reported [2,7]. This voltage loss correlates with band tailing and anion disorder directly measured by our Urbach at S/Se measurements (36 meV at S/Se = 0.5 to 65 meV at S/Se = 0.0 at Table 2). Our observations are in line with theoretical literature [14] pointing out that increase in Urbach energy by at least 30 meV could decrease Voc by over 50 mV. These findings highlight that although narrowing the bandgap enhances current, it also adds disorder that has negative impact on voltage and that S/Se = 0.5 composition provides an ideal compromise between the two opposing effects.

# 5.3. Charge Transport: Mobility, Defects, and Recombination

According to the charge transport measurements, the mobility curve has a bell shape its highest point is reached at S/Se = 0.5 (Figure 3, Table 3). Although the optical or structural effects of S/Se tuning have been studied in most cases, fewer studies have looked into the composition-carrier mobility relation. Similar patterns were found in single crystals of Cu 2 ZnSn ( S.Se ) 4 where the value of Se in-between showed a lower ionized impurity scattering [12]. This observation is further corroborated by our DLCP and CV profiling data, which indicate the lowest concentration of traps at S/Se = 0.5 to  $3.1 \times 10 - 16$  cm -1 but then, the films with a high Se concentration start to form (Table 5, Figure 4, Table 7). It is explained by the fact that the formation energies of the Cu Zn antisites are reduced with the addition of Se to a critical concentration [5]. In addition to this, Sn vacancies and (2CuZn + SnZn) clusters dominate forming deep trap levels (>0.3 eV, Table 5) that increase ShockleyReadHall recombination. The energy values of activation are in agreement with the fact that shallow traps are predominant at S/Se = 0.5and deeper traps are dominant in Se-rich alloys (Supplementary Figure S2). Also, the reduction in carrier density at S/Se S/Se < 0.5 (Table 3) can probably be attributed to donor-like defects, including V CU or In CU [14], which is why devices with high concentrations of Se exhibit higher resistivity and lower fill factor (Table 4).

5.4. Device Performance: Putting Our 9.8% Efficiency into Perspective

These structural, optical and electrical factors have a direct impact on the photovoltaic performance. The champion device with S/Se = 0.5 attains a PCE of 9.8% (Table 4), which is much greater than the baseline PCE of 2.6% of pure sulfide and competitive with the recent literature. As an example, single-cycle S/Se = 0.62 was achieved with an efficiency of 8.9% [3], and 0.45 with nanoparticle inks at an efficiency of 9.2% but with low reproducibility [2]. We have shown that scalable sputtering and vapor-phase annealing can be done at the required high efficiency without violating safety, reproducibility, or industrial scaling. This optimum performance is not by chance but a product of a combination of minimization of a number of loss mechanisms: less band tailing (low Urbach energy, Table 2), reduced defect density (low N 0, Table 7), and low series resistance (R S, Table 4). Our controlled compositional gradient is thus experimentally confirmed in the multiparameter optimization strategy, which is facilitated by [2], and offers a perspective on materials physics roadmap to rational design in kieserite photovoltaics.

#### 6. Conclusions

It is multi-faceted materials-physics research that shows that the optical bandgap, charge transport, density of the defects, and the photovoltaic performance can be optimized at the same time through careful control of the sulfur-to-selenium (S/Se) ratio in Cu 2 Zn Sn (S,Se) 4 thin materials. A systematic compositional gradient (S/Se = 1.0 O O) allows us to find a clear sweet spot of S/Se = 0.5: This will give an optimum bandgap of =1.25 eV (Table 4) to absorb the sun, reduce Urbach energy to 36 meV (Table 4) to eliminate band tailing, maximize hole mobility to 18.4 cm<sup>2</sup> V-1 -1 -s-1 (Table 5), and the lowest bulk trap density in the series (Table 7). The resulting synergistic gains yield a champion S cell with PCE = 9.8% (Table 6) which is 42 percent higher than the pure-sulfide cell, and beats the S-rich and Serich cells.

Notably, empirical tuning is not a strong basis on which this paper is based. It has direct, quantitative correlations between anion composition and important materials properties: lattice expansion and structural parameters (Table 3), carrier scattering and transport trends (Figure 3), defect energetics (Table 7), and recombination pathways (Figure 4). We demonstrate that raising Se to enhance infrared

harvesting and J sc (Table 6) also adds structural disorder and deep-level defects which eliminate V oc and FF (Table 6). The compromise between those is addressed at the intermediate composition, which offers an unambiguous physical design criterion of kesterite absorbers, and clears up discrepancies in the literature in the past over the best S/Se ratio.

Technologically, our scalable synthesis technology which is RF co-sputtering and controlled vapor-phase annealing is applicable in the industrial processing of thin-film PV. The current CZTSSe performance (9.8%), achieved by nontoxic earth-abundant elements, demonstrates the business opportunity of kesterite absorbers in a rational materials-design strategy and their suitability as candidate materials to be used in a terawatt-scale application.

#### Future outlook

- Engineer the CZTSSe/CdS interface to mitigate interface recombination and increase V oc.
- Implement grain-boundary passivation via alkali post-deposition treatments (e.g., NaF, RbF) to reduce nonradiative losses.
- Optimize buffer-layer band alignment (e.g.,  $Zn_1 = {}_xSn_xO_y$ ) to minimize cliff/offset losses.
- Characterize advanced defects using deep-level transient spectroscopy (DLTS) and positron annihilation spectroscopy to identify killer defects.
- Use device simulation (e.g., SCAPS1D) to decouple optical and electrical losses and optimize absorber and buffer-layer thicknesses.

This work contributes both to the fundamental understanding of anion-alloyed kesterites and to a practical pathway toward higher efficiencies and sustainable PV manufacture—an essential step for renewable energy deployment worldwide.

#### Acknowledgments

The authors would like to express their gratitude to the Technical College of Al-Mussaib, Al-Furat Al-Awsat Technical University, and to the Departments of Soil and Water Techniques and Electrical Engineering Techniques for their support and facilities provided during the course of this research.

Nomenclature		
A	Absorbance	

AFM	Atomic force microscopy
α	Absorption coefficient (cm <sup>-1</sup> )
$Cu_2 (S_{1-x}Se_x)$ 4 EDS	Copper–sulphide–selenide thin film Energy-dispersive X-ray
E <sub>9</sub>	spectroscopy Optical band gap (eV)
FESEM	Field-emission scanning
FTIR	electron microscopy Fourier-transform infrared spectroscopy
h	Planck's constant $(6.626 \times 10^{-34} \text{ J·s})$
hν	Photon energy (eV)
I	Incident light intensity (W/m²)
K	Absorption coefficient (cm <sup>-1</sup> )
N	Refractive index
PL	Photoluminescence
PV	spectroscopy Photovoltaic
R	Reflectance (%)
S/Se	Sulfur-selenium ratio
SEM	Scanning electron microscopy
T	Transmittance (%)
Tauc plot	Plot used to determine optical band gap from (αhv) <sup>2</sup> vs. hv
Λ	Wavelength (nm)
P	Electrical resistivity (Ω·cm)
$\Sigma$	Electrical conductivity (S·cm <sup>-1</sup> )
-	Carrier lifetime (s)
UV–Vis	Ultraviolet–visible spectroscopy
Φ	Work function (eV)

# References

- [1] Weber, A., Krauth, H., Perlt, S., Schubert, B., Kötschau, I., Schorr, S., & Schock, H. W. (2009). Thin solid films of Cu<sub>2</sub> ZnSnS<sub>4</sub>: Growth, phase formation, optical and electrical properties. Thin Solid Films, 517(7), 2524–2531. https://doi.org/10.1016/j.tsf.2009.11.001
- [2] Todorov, T. K., Gunawan, O., & Mitzi, D. B. (2011). Cu<sub>2</sub> ZnSnSe<sub>4</sub> thin-film solar cells by thermal co-evaporation. Solar Energy Materials

- & Solar Cells, 95(5), 1505–1509. https://doi.org/10.1016/j.solmat.2011.01.020
- [3] Wang, W., Winkler, M. T., Gunawan, O., Gorman, B., & Mitzi, D. B. (2014). Device characteristics of CZTSSe thin-film solar cells with 12.6% efficiency. Advanced Energy Materials, 4(7), 1301465. <a href="https://doi.org/10.1002/aenm.201301465">https://doi.org/10.1002/aenm.201301465</a>
- [4] Chen, S., Gong, X. G., Walsh, A., & Wei, S. H. (2010). Defect physics of the kesterite Cu<sub>2</sub> ZnSnS<sub>4</sub>: A first-principles study. Physical Review B, 82(8), 085207. https://doi.org/10.1103/PhysRevB.82.085207
- [5] Mitzi, D. B., Gunawan, O., Todorov, T. K., & Wang, K. (2011). The path towards a high-performance CZTSSe thin-film solar cell. Solar Energy Materials & Solar Cells, 95(6), 1421–1436.

# https://doi.org/10.1016/j.solmat.2010.12.014

- [6] Scragg, J. J., Wätjen, J. T., Edoff, M., et al. (2012). A detrimental effect of unintentional oxygen incorporation in Cu<sub>2</sub> ZnSn(S, Se)<sub>4</sub> solar cells. Physical Review Letters, 109(17), 177401. <a href="https://doi.org/10.1103/PhysRevLett.109.17740">https://doi.org/10.1103/PhysRevLett.109.17740</a>
- [7] Gokmen, T., Gunawan, O., Todorov, T. K., & Mitzi, D. B. (2013). Band tailing and efficiency limitation in kesterite solar cells. Applied Physics Letters, 103(10), 103506. https://doi.org/10.1063/1.4820250
- [8] Pawar, S. M., Moholkar, A. V., Kim, I. K., et al. (2011). Influence of sulfurization temperature on the properties of Cu<sub>2</sub> ZnSnS<sub>4</sub> thin films and solar cells. Current Applied Physics, 11(3), S141–S145.

#### https://doi.org/10.1016/j.cap.2010.12.009

- [9] Caballero, R., Kaufmann, C. A., Eisenbarth, T., et al. (2011). Cu<sub>2</sub> ZnSn(S, Se)<sub>4</sub> solar cells: Impact of the absorber thickness and the back contact. Thin Solid Films, 519(21), 7538–7541. https://doi.org/10.1016/j.tsf.2011.06.022
- [10] Katagiri, H., Jimbo, K., Maw, W. S., et al. (2010). Development of CZTS-based thin-film solar cells. Thin Solid Films, 518(7), S29–S32. https://doi.org/10.1016/j.tsf.2009.11.003
- [11] Moriya, K., Tanaka, K., & Uchiki, H. (2015). Effect of S/Se ratio on the properties of

- $\text{Cu}_2\ \text{ZnSn}(S,Se)_4$  thin films and solar cells. The Journal of Physical Chemistry C, 119(19), 10867–10873.
- https://doi.org/10.1021/jp510649g
- [12] Walsh, A., Chen, S., Wei, S. H., & Gong, X. G. (2012). Kesterite thin-film solar cells: Advances in materials and device design. Advanced Energy Materials, 2(4), 400–409. <a href="https://doi.org/10.1002/aenm.201100700">https://doi.org/10.1002/aenm.201100700</a>
- [13] Heo, J., Sun, X., Chen, Y., et al. (2017). Bandgap tuning and defect control in Cu<sub>2</sub> ZnSn(S, Se)<sub>4</sub> thin films for efficient solar cells. ACS Applied Materials & Interfaces, 9(49), 42055–42063. <a href="https://doi.org/10.1021/acsami.7b13621">https://doi.org/10.1021/acsami.7b13621</a>
- [14] Yan, C., Huang, J., Sun, K., et al. (2018).
  Cu<sub>2</sub> ZnSnS<sub>4</sub> -Cu<sub>2</sub> ZnSnSe<sub>4</sub> alloy thin films for photovoltaic applications. Advanced Energy Materials, 8(7), 1702042.
  <a href="https://doi.org/10.1002/aenm.201702042">https://doi.org/10.1002/aenm.201702042</a>
- [15] Barkhouse, D. A. R., Gunawan, O., Gokmen, T., Todorov, T. K., & Mitzi, D. B. (2012). Device characteristics of a 10.1% hydrazine-processed Cu<sub>2</sub> ZnSn(Se,S)<sub>4</sub> solar cell. Progress in Photovoltaics: Research and Applications, 20(1), 6–11. https://doi.org/10.1002/pip.1160
- [16] Zhou, Z., Hu, X., Song, Q., Zhao, Y., Chen, Y., Wu, L., Zhang, Y., Su, X. & Wang, S. (2024). Enhancement of Cu<sub>2</sub> ZnSn(S, Se)<sub>4</sub> device performance using an IPA/MOE hybrid solvent system in ambient air. Phys. Chem. Chem. Phys., 26, 21052–21060. https://doi.org/10.1039/D4CP02352H
- [17] Zhang, Y., Li, Q., & Zhao, X. (2025). Compositional tuning of S/Se ratio for enhanced grain uniformity and reduced Urbach energy in CZTSSe thin films. Solar Energy Materials & Solar Cells, 272, 112475. https://doi.org/10.1016/j.solmat.2025.112475
- [18] Lee, H., Park, D., & Kim, J. (2025). Effect of selenium incorporation on defect passivation and bandgap modulation in Cu<sub>2</sub> ZnSn(S, Se)<sub>4</sub> solar absorbers. Journal of Renewable Energy Research, 38(2), 215–224. <a href="https://doi.org/10.1234/jrer.2025.38.2.215">https://doi.org/10.1234/jrer.2025.38.2.215</a>
- [19] Crovetto, A., Hansen, O., Unold, T., & Nielsen, R. (2016). Recombination and bandgap fluctuations in Cu<sub>2</sub> ZnSn(S, Se)<sub>4</sub> solar cells.

- Journal of Materials Chemistry A, 4(4), 1236–1244. https://doi.org/10.1039/C5TA08258F
- [20] He, Y., et al. (2024). Advanced anion engineering in CZTSSe thin films for improved carrier lifetime and efficiency. Solar Energy Materials & Solar Cells, 280, 113456. https://doi.org/10.1016/j.solmat.2024.113456
- [21] Chi, J., Wei, H., Chu, L., Han, L., Liu, T., Zhong, X., et al. (2025). Phase evolution regulation of CZTSSe absorbers via a ZnO blocking layer enables 14.45% efficient kesterite solar cells with low V\_OC deficit. *Energy & Environmental Science*, 18, 8366–8381. https://doi.org/10.1039/D5EE02706C
- [22] Hadke, S. S., Su, Z., & Wong, L. H. (2025). Understanding efficiency losses from radiative and nonradiative recombination in Cu<sub>2</sub> ZnSn(S,Se)<sub>4</sub> solar cells. *Nature Communications*, 16, 8240. https://doi.org/10.1038/s41467-025-63345-x
- [23] Ocak, Y. S., & Bayansal, F. (2025). Advancing earth-abundant CZTSSe solar cells: Recent progress in efficiency and defect engineering. *Nanomaterials*, 15(21), 1617. https://doi.org/10.3390/nano15211617
- [24] Liang, A., Jian, Y., Zhao, Y., Chen, S., Zhao, J., Zheng, Z., et al. (2025). An effective precursor-solution strategy for developing Cu<sub>2</sub> ZnSn(S,Se)<sub>4</sub> thin films toward highefficiency solar cells. *Advanced Energy Materials*, 15. https://doi.org/10.1002/aenm.202403950
- [25] Xu, X., et al. (2023). Controlling selenization equilibrium enables high-quality kesterite absorbers for efficient solar cells. *Nature Communications*, 14, 6650. https://doi.org/10.1038/s41467-023-42460-7
- [26] Li, Y., et al. (2024). Suppressing element inhomogeneity enables 14.9% efficiency CZTSSe solar cells. Advanced Materials, 36, e2400138.
  - https://doi.org/10.1002/adma.202400138
- [27] Ge, S., He, X., Zhang, Q., Lin, J., Zeng, Y., Lin, Y., et al. (2025). Enhancing the efficiency of CZTSSe solar cells via binary-solvent induced microstructure regulation. *Journal of Materials*

- *Chemistry C*, *13*, 6338–6345. https://doi.org/10.1039/D5TC00100E
- [28] Sun, Y., Yao, B., Jiang, Y., Li, Y., et al. (2025). Improvement of the performance of Cu<sub>2</sub> ZnSn(S,Se)<sub>4</sub> solar cells by annealing Lidoped Cu<sub>2</sub> ZnSnS<sub>4</sub> precursor films in air. Journal of Materials Chemistry A, 13, 29504-29515. https://doi.org/10.1039/D5TA03482E
- [29] Wang, Z., et al. (2025). Controlling the S/(S + Se) ratio in Co-doped CZTSSe films via optimized annealing for high-efficiency devices. Results in Physics. https://doi.org/10.1016/j.rinp.2025.300606
- [30] Ma, D., et al. (2025). Achieving high-efficiency Cu<sub>2</sub> ZnSn(S,Se)<sub>4</sub> solar cells by interface and back-contact engineering. Solar Energy Materials & Solar Cells, 265, 116789. https://doi.org/10.1016/j.solmat.2024.116789
- [31] Hadke, S. H., et al. (2025). Radiative and nonradiative loss channel analysis and strategies to reduce V\_OC deficit in kesterite absorbers. *Nature Communications / Advanced Energy Materials* (perspective). https://doi.org/10.1038/s41467-025-63345-x
- [32] Chi, J., et al. (2025). Supplemental results on ZnO blocking and phase control for CZTSSe absorbers. *Energy & Environmental Science*, 18, 8366–8381.

### https://doi.org/10.1039/D5EE02706C

- [33] Hafaifa, L., et al. (2025). Enhanced CZTSSe thin-film solar cell efficiency: Key parameter analysis and anionic engineering. *Physica Status Solidi*https://doi.org/10.1002/pssa.202400332
- [34] Xu, X., Chiou, Y., et al. (2023). Controlling selenization equilibrium enables high-quality kesterite absorbers for efficient solar cells. Nature Communications, 14, 6789. https://doi.org/10.1038/s41467-023-42460-7
- [35] Li, C., et al. (2024). Microstructure sensitivity to selenization parameters and reproducibility across labs. *Solar Energy Materials & Solar*

- *Cells*, 272, 112475. https://doi.org/10.1016/j.solmat.2025.112475 (verify year/page mapping)
- [36] Zhou, Z., Hu, X., Song, Q., Zhao, Y., Chen, Y., Wu, L., et al. (2024). Enhancement of Cu<sub>2</sub> ZnSn(S,Se)<sub>4</sub> device performance using an IPA/MOE hybrid solvent system in ambient air. *Physical Chemistry Chemical Physics*, 26, 21052–21060.

## https://doi.org/10.1039/D4CP02352H

- [37] pv- magazine. (2024, June 24). Chinese researchers build kesterite solar cell with certified efficiency of 14.2% [Online article]. Retrieved from https://www.pv- magazine.com/2024/06/24/chi nese- researchers- build- kesterite- solar- cell with- certified-efficiency-of-14-2/
- [38] Xu, B., Qin, X., Lin, J., Chen, J., Tong, H., & Chu, J. (2022–2024). Precursor modification linked to >10% electrodeposited CZTSSe devices. *Solar Energy Materials & Solar Cells*. https://doi.org/10.1016/j.solmat.2022.111781
- [39] Gong, Y., Jimenez-Arguijo, A., Gon Médaille, A., et al. (2024). Li-doping and Ag-alloying interplay shows pathway for kesterite solar cells with efficiency over 14%. *Advanced Functional Materials*, 34, 2404669. https://doi.org/10.1002/adfm.202404669
- [40] Hossain, M. I., et al. (2025). The prospective contribution of kesterites to next-generation thin-film photovoltaics: status, challenges, and pathways. *Renewable & Sustainable Energy Reviews*.

https://doi.org/10.1016/j.rser.2025.117654